Research Square

Preprints are preliminary reports that have not undergone peer review.
They should not be considered conclusive, used to inform clinical practice,
or referenced by the media as validated information.

An Fe–Ti bimetallic MOF-functionalized electrospun PVDF-HFP separator for homogeneous Li^+ flux in thermally robust, fast-charging $LiFePO_4$ batteries

Keying Wu

kywu601@163.com

Application Research Center of Smart Energy Technology of Mianyang City College

Wenda Xie

Application Research Center of Smart Energy Technology of Mianyang City College

Xingjian Liu

Meishan Vocational & Technical College

Jing Chen

Meishan Vocational & Technical College

Haitao Pu

Meishan Vocational & Technical College

Bing Luo

Application Research Center of Smart Energy Technology of Mianyang City College

Research Article

Keywords: Fe–Ti bimetallic MOF, electrospun separator, Li+ flux regulation, LiFePO4 batteries

Posted Date: September 10th, 2026

DOI: https://doi.org/10.21203/rs.3.rs-10497963/v1

License: This work is licensed under a Creative Commons Attribution 4.0 International License.
Read Full License

Additional Declarations: No competing interests reported.

Abstract

Lithium iron phosphate ($LiFePO_4$, LFP) batteries dominate the electric-vehicle and stationary-storage markets, yet fast charging at elevated temperature places stringent demands on the separator, particularly its ability to regulate Li^+ flux. Commercial polyolefin separators act only as inert physical barriers and suffer from severe thermal shrinkage and poor wettability, aggravating dendrite growth at high rates. Herein, an Fe–Ti bimetallic metal–organic framework (Fe–Ti MOF) was synthesized via a facile solvothermal route and incorporated into poly(vinylidene fluoride-co-hexafluoropropylene) (PVDF-HFP) nanofiber membranes through one-step electrospinning to construct multifunctional composite separators. Benefiting from the abundant open metal sites and Lewis-acidic Fe/Ti centers, the bimetallic MOF strongly anchors PF_6^- anions and homogenizes the Li^+ flux across the separator. The optimized PVDF-HFP/MOF-10 separator exhibits a low electrolyte contact angle of 18°, an ionic conductivity of 1.7×10^{-3} S cm^{-1}, and an enhanced Li^+ transference number of 0.56 (vs. 0.24 for Celgard), together with a thermal shrinkage of only 5.8% at 160°C. Consequently, Li||Li symmetric cells deliver stable plating/stripping for over 500 h at 1 mA cm^{-2}, and $LiFePO_4$||Li cells achieve an initial discharge capacity of 153 mAh g^{-1} at 1 C, retain 118 mAh g^{-1} at 10 C, deliver 92.3% capacity retention over 500 cycles at 1 C with average Coulombic efficiency > 99.8%, and sustain nearly unattenuated capacity up to 80°C, substantially outperforming Celgard- and pristine PVDF-HFP-based cells. This work demonstrates that bimetallic-site engineering of MOF-functionalized separators is an effective anion-anchoring and Li^+-flux-homogenization strategy for safe, fast-charging lithium batteries.

1. Introduction

The ever-growing demand for portable electronics, electric vehicles, and grid-scale energy storage has continuously pushed lithium-ion batteries (LIBs) toward higher energy densities [1–3]. Among various cathode materials, olivine $LiFePO_4$ (LFP) has become the dominant choice for electric vehicles and grid-scale storage owing to its intrinsic thermal stability, long cycle life, low cost, and cobalt-free composition [4, 5]. However, the strong P–O covalent framework that underpins this stability also imposes intrinsically low electronic and ionic conductivity; under fast charging and at elevated temperature this intensifies concentration polarization and heterogeneous Li^+ deposition on the anode side, raising serious concerns over rate capability, cycle life, and safety [6–8]. In our previous work on cathode interfacial engineering [9], we demonstrated that a $Li_2Zr(PO_4)_2$ heterojunction coating can stabilize the cathode–electrolyte interface and markedly improve capacity retention; nevertheless, cathode-side modification alone cannot resolve the cell-level safety and dendrite issues, and the separator—an often overlooked component—plays an equally decisive role.

Commercial polyolefin separators (e.g., polypropylene (PP) Celgard) benefit from low cost and good mechanical strength, but their intrinsic drawbacks are increasingly incompatible with fast-charging, wide-temperature operation: severe thermal shrinkage above 110°C, poor wettability toward polar carbonate electrolytes, and low porosity restrict both ion transport and safety margins [10–12]. More

fundamentally, polyolefin separators act only as inert physical barriers and possess no capability to regulate ionic transport. A growing consensus holds that next-generation separators should function as active regulators of ion flux rather than passive spacers, and a variety of functionalized separators based on functional coatings, grafted surface layers, and polymer blending have been developed accordingly [13–15].

Electrospun poly(vinylidene fluoride-co-hexafluoropropylene) (PVDF-HFP) membranes are attractive separator matrices because of their interconnected three-dimensional porous networks, high porosity (70–90%), excellent electrolyte uptake, and the strong polarity of C–F bonds that favors interaction with electrolyte molecules and lithium salts [16–18]. Nonetheless, pristine electrospun PVDF-HFP separators still suffer from insufficient mechanical strength and thermal dimensional stability, and, similar to polyolefins, they lack active sites to homogenize Li^+ flux, which limits their performance in dendrite suppression and high-rate full cells [19, 20].

Metal–organic frameworks (MOFs), with their ordered sub-nanometer channels, ultrahigh surface areas, and tailorable open metal sites, have recently emerged as powerful separator modifiers [21–23]. The angstrom-scale micropores of MOFs can sieve solvated species, while the Lewis-acidic metal centers spontaneously anchor PF_6^- anions, thereby immobilizing anion motion, elevating the Li^+ transference number (t_{Li}^+), and homogenizing the Li^+ flux arriving at the anode surface [24–26]. However, the regulation capability of single-metal MOFs is constrained by the fixed electronic structure and limited Lewis acidity of a single type of metal node. Bimetallic MOFs, in which two metal centers coexist within one framework, offer synergistic effects—modulated charge distribution, enriched unsaturated sites, and enhanced structural robustness—as demonstrated in various bimetallic frameworks for energy-storage and separator applications [27–29].

Fe is a particularly appealing partner metal: it is earth-abundant and inexpensive, possesses accessible Fe^{2+}/Fe^{3+} redox states that enrich the electronic structure of the framework, and exhibits strong Lewis acidity favorable for anion anchoring [30, 31]. Despite these merits, to the best of our knowledge, Fe–Ti bimetallic MOFs have not yet been explored as functional fillers in electrospun separators, and their applicability to LFP systems remains unreported. Whether the Fe–Ti dual sites can cooperatively strengthen PF_6^- anchoring and Li^+ flux homogenization, and thus simultaneously address the thermal-safety and dendrite issues under fast-charging operation, is an open and practically important question.

Herein, we report a one-step electrospun PVDF-HFP separator functionalized with a solvothermally synthesized Fe–Ti bimetallic MOF for $LiFePO_4$ batteries. The bimetallic composition and single-particle Fe/Ti co-localization were rigorously verified by XRD, XPS, TEM-EDS, and ICP-OES. The optimized PVDF-HFP/MOF-10 separator combines superior thermal dimensional stability (5.8% shrinkage at 160°C), excellent electrolyte affinity (contact angle 18°), a high ionic conductivity of 1.7×10^{-3} S cm^{-1}, and an elevated t_{Li}^+ of 0.56. As a result, Li||Li symmetric cells operate stably for over 500 h, and $LiFePO_4$||Li cells

deliver 153 mAh g^{-1} at 1 C together with excellent rate capability up to 10 C and stable operation up to 80°C, revealing the effectiveness of the bimetallic anion-anchoring and flux-homogenization mechanism.

2. Experimental section

2.1 Materials

PVDF-HFP (Mw = 400,000, Sigma-Aldrich), terephthalic acid (H_2BDC, 99%, Aladdin), titanium(IV) isopropoxide (TTIP, 97%, Aladdin), iron(III) nitrate nonahydrate ($Fe(NO_3)_3·9H_2O$, 98%, Aladdin), acetic acid (AR, Sinopharm Chemical Reagent Co., Ltd.), N,N-dimethylformamide (DMF, AR, Sinopharm), anhydrous methanol (AR, Sinopharm), and acetone (AR, Sinopharm) were used as received without further purification. The electrolyte (1 M $LiPF_6$ in EC/DMC/EMC (v/v/v = 1:1:1) with 2 wt% VC, Guotai Huarong), $LiFePO_4$ cathode sheets (Shenzhen Kejing Star Technology Co., Ltd., areal loading ~ 3.2 mg cm^{-2}), lithium foil (99.9%, Zhongneng Lithium Industry), and Celgard 2400 were purchased from the corresponding suppliers.

2.2 Sample preparation

2.2.1 Synthesis of the Fe–Ti bimetallic MOF. In a typical procedure, 3.0 g of H_2BDC (~ 18.1 mmol) was dissolved in a mixed solvent of DMF (54 mL) and anhydrous methanol (6 mL) (v/v = 9:1) under stirring at room temperature for 30 min until a completely clear solution was obtained. Subsequently, 0.27 g of $Fe(NO_3)_3·9H_2O$ (~ 0.67 mmol, corresponding to 10 mol% of the total metal content) was added to the ligand solution together with 1 mL of acetic acid as a modulator, and the mixture was stirred for another 30 min to allow the pre-coordination of Fe^{3+} with the carboxylate ligand and acetate species, which proved essential for the successful incorporation of Fe into the framework. Then, 1.8 mL of TTIP (~ 6.1 mmol) was added dropwise, and the solution was further stirred for 1 h, giving a ligand-to-total-metal molar ratio of ~ 2.7:1 and a nominal Fe:Ti molar ratio of ~ 1:9. The resulting homogeneous solution was transferred into a 100 mL Teflon-lined stainless-steel autoclave (filling degree ≤ 70%), heated at 150°C for 24 h, and then cooled naturally to room temperature. The precipitate was collected by centrifugation, washed with DMF three times to remove the residual ligand and then with methanol three times for solvent exchange, and finally dried at 60°C under vacuum for 12 h to obtain the Fe–Ti MOF as a white to pale-yellow powder.

2.2.2 Synthesis of single-metal control MOFs. The single-metal Ti-MOF (MIL-125(Ti)) and the Fe-based control were synthesized via the same solvothermal protocol in the absence of the second metal source, serving as control samples.

2.2.3 Fabrication of composite separators. PVDF-HFP powder was dissolved in a DMF/acetone mixed solvent (7:3, w/w) to form a 10 wt% spinning solution. A prescribed amount of Fe–Ti MOF (5, 10, or 15 wt% relative to PVDF-HFP) was dispersed in the solution by ultrasonication for 1 h and stirring for 24 h. Electrospinning was performed at an applied voltage of 18 kV, a feed rate of 1.2 mL h^{-1}, a needle-to-collector distance of 15 cm, and a drum rotation speed of 300 rpm (25°C, 30% relative humidity). The as-spun membranes were vacuum-dried at 60°C for 12 h and pressed to a controlled thickness of ~ 25 μm.

The resulting separators are denoted as PVDF-HFP, PVDF-HFP/MOF-5, PVDF-HFP/MOF-10, and PVDF-HFP/MOF-15 according to the MOF loading.

2.3 Material characterizations

The crystalline phases were examined by X-ray diffraction (XRD, Bruker D8 Advance, Cu Kα) and compared with the simulated pattern of MIL-125(Ti) (CCDC 809174). Raman spectra were recorded on a Renishaw inVia spectrometer with a 532 nm laser, and FT-IR spectra on a Nicolet iS50 spectrometer. The surface chemical states (Fe 2p, Ti 2p, O 1s) were probed by X-ray photoelectron spectroscopy (XPS, Thermo ESCALAB 250Xi), and the actual Fe:Ti ratio was quantified by inductively coupled plasma optical emission spectrometry (ICP-OES, Agilent 720ES). Morphologies and elemental distributions were observed by field-emission scanning electron microscopy (SEM, Hitachi SU8010) and transmission electron microscopy (TEM, FEI Tecnai G2 F20) equipped with EDS mapping, including single-particle Fe/Ti co-localization. The specific surface area and pore-size distribution were measured by N_2 adsorption–desorption (Micromeritics ASAP 2460). Electrolyte contact angles were measured in triplicate on a DataPhysics OCA20 instrument. Thermal stability was evaluated by thermogravimetric analysis (TGA, TA Q500, N_2, 30–800°C, 10°C min^{-1}), thermal-shrinkage tests (holding at each temperature for 1 h), FLIR thermal imaging, and combustion tests. Mechanical properties were assessed by tensile stress–strain measurements (Instron 5967, stretching rate 5 mm min^{-1}).

2.4 Electrochemical measurements

The ionic conductivity (σ) was measured by temperature-dependent electrochemical impedance spectroscopy (EIS) on SS|separator|SS cells and calculated as $\sigma = d/(R_b \cdot S)$, where d is the separator thickness, R_b the bulk resistance, and S the effective area. The Li^+ transference number was determined on Li|separator|Li cells by the Bruce–Vincent method with a DC polarization of 10 mV, $t_{Li^+} = I_s(\Delta V - I_o R_o)/[I_o(\Delta V - I_s R_s)]$. Galvanostatic Li plating/stripping was carried out on Li||Li symmetric cells at 1 mA cm^{-2} with a capacity of 1 mAh cm^{-2}; cycled cells were disassembled in the glovebox for post-mortem characterization. CR2032 $LiFePO_4$||Li half cells (voltage window 2.5–4.0 V) were assembled in an Ar-filled glovebox (H_2O, O_2 < 0.1 ppm) and tested for initial charge–discharge behavior, rate capability (1–10 C), long-term cycling at 1 C with Coulombic efficiency, cyclic voltammetry (CV, 0.1 mV s^{-1}), EIS before and after cycling, and temperature-dependent discharge (20–80°C).

2.5 Theoretical calculations

Spin-polarized density functional theory (DFT) calculations were performed using the VASP package with the PBE-GGA functional and the projector-augmented wave (PAW) method, a plane-wave cutoff energy of 450 eV, a 3 × 3 × 1 Monkhorst–Pack k-point mesh, and DFT-D3 dispersion correction. Structures were relaxed until the residual forces were below 0.02 eV $Å^{-1}$ with an energy convergence criterion of 10^{-5} eV; full computational details are provided in the Supporting Information. The adsorption energies (E_ads) of PF_6^-, Li^+, and electrolyte molecules (EC and DMC) on PP, PVDF-HFP

(CH_2CF_2, CH_3CF_2H, and HFP units), and the Fe–Ti MOF surfaces were calculated as $E_{ads} = E_{total} - E_{substrate} - E_{adsorbate}$, where more negative values indicate stronger adsorption.

3. Results and discussion

3.1 Structure and morphology of the Fe–Ti bimetallic MOF

The crystalline structure of the as-synthesized MOFs was first examined by XRD (Fig. 1a). The diffraction pattern of the Fe–Ti MOF matches well with the simulated pattern of MIL-125(Ti) and the single-metal Ti-MOF control, with characteristic peaks at 6.8°, 9.7°, and 11.7°, indicating that the incorporation of Fe does not destroy the framework topology. Notably, a slight shift of 0.13° toward lower angles is observed for the bimetallic sample, suggesting lattice expansion induced by the partial substitution of Ti^{4+} (ionic radius 0.605 Å) by the larger Fe^{3+} (0.645 Å). Raman (Fig. 1b) and FT-IR (Fig. 1c) spectra further confirm the framework integrity: the bands at 1612 and 1438 cm^{-1} are assigned to the aromatic ring stretching and carboxylate vibrations of the BDC linkers, respectively, while the fingerprint band at 550 cm^{-1} corresponds to the Ti–O/Fe–O vibration. SEM images (Fig. 1f) show that the Fe–Ti MOF inherits the typical disc-like (tablet) morphology of MIL-125(Ti) with a uniform particle size of ~ 300–500 nm, which is favorable for its subsequent dispersion within the electrospun fibers.

The coexistence and valence states of the two metals—the evidential foundation of this work—were verified by combined XPS, TEM-EDS, and ICP-OES analyses. In the high-resolution Fe 2p spectrum (Fig. 1d), the peaks at 711.5 and 725.0 eV are attributed to Fe $2p_{3/2}$ and Fe $2p_{1/2}$ of Fe^{3+} (with a satellite at 719.0 eV), while the Ti 2p spectrum (Fig. 1e) shows Ti $2p_{3/2}$/Ti $2p_{1/2}$ peaks at 458.5 and 464.2 eV, characteristic of Ti^{4+} in an octahedral O environment. Compared with the single-metal controls, the Ti 2p (Fe 2p) binding energies shift by 0.3 eV, evidencing electron redistribution between the Fe and Ti centers and thus their intimate electronic coupling rather than a physical mixture. Single-particle EDS mapping (Fig. 1g) reveals the homogeneous co-localization of Fe and Ti throughout an individual crystal, and ICP-OES gives an actual Fe/Ti atomic ratio of 0.108 (i.e., ~ 1:9.3), close to the nominal feed ratio of 1:9. TGA (Fig. 1h) shows that the framework is thermally stable up to 365°C, and N_2 sorption analysis yields a specific surface area of 1268 $m^2\ g^{-1}$ with a micropore size centered at 0.76 nm (Fig. S1), smaller than the solvation sheath of Li^+ yet accessible to bare ions—an ideal geometry for ion sieving.

3.2 Microstructure and mechanical properties of the composite separators

Surface SEM images (Fig. 2a–d) show that all separators consist of randomly interwoven, bead-free nanofibers forming interconnected porous networks; the MOF particles are uniformly anchored on and within the fibers without blocking the pores. The cross-sectional image (Fig. 2e) confirms a uniform thickness, and the magnified views (Fig. 2f, g) further reveal the intimate integration of the Fe–Ti MOF with the PVDF-HFP matrix. EDS mapping of the PVDF-HFP/MOF-10 separator (Fig. 2h–k) demonstrates

the homogeneous distribution of C, F, Ti and Fe over the membrane, confirming that the framework is incorporated intact rather than decomposed during electrospinning.

3.3 Thermal safety and flame retardancy

TGA curves (Fig. 3a) show that the Celgard separator starts to decompose at 410°C and decomposes almost completely with negligible residue, whereas the electrospun PVDF-HFP membranes decompose mainly within 450–490°C. For the composite separators, a minor mass loss appears above ~ 365°C, originating from the decomposition of the organic linkers of the embedded MOF, while the main decomposition stage of the polymer matrix shifts upward by ~ 10°C; the residual mass at 800°C increases from 27% to 35.2%, indicating that the inorganic framework acts as a thermal stabilizer that absorbs heat and retards chain degradation. Thermal-shrinkage tests (Fig. 3b) provide the most safety-relevant contrast: after holding at 160°C for 1 h, Celgard shrinks drastically by 71% with evident melting, and pristine PVDF-HFP still shrinks by 46%, whereas PVDF-HFP/MOF-5/10/15 shrink by only 14.7%, 5.8%, and 2.2%, respectively, showing a monotonic improvement with MOF content.

FLIR imaging (Fig. 3c) confirms the uniform in-plane heat distribution of the composite separators from 30 to 170°C, and at 170°C the MOF-modified membranes preserve their dimensional integrity while Celgard has completely melted. In combustion tests (Fig. 3d), Celgard shrinks within 0.5 s and burns violently at 0.8 s; in contrast, the PVDF-HFP/MOF separators exhibit markedly retarded ignition (3.2 s) and self-extinguishing behavior, which is ascribed to the intrinsic flame resistance of the fluorinated matrix combined with the heat-absorbing barrier effect of the MOF filler. These results collectively demonstrate that the Fe–Ti MOF endows the separator with strong resistance against thermal runaway.

3.4 Electrolyte affinity and ion-transport kinetics

Electrolyte wettability was evaluated by contact-angle measurements (Fig. 4a, in triplicate). The contact angle decreases from 61 ± 7° for Celgard and 28 ± 4° for pristine PVDF-HFP to only 18 ± 2° for PVDF-HFP/MOF-10, owing to the polar C–F matrix, the porous fibrous architecture, and the strong affinity of the MOF open metal sites toward carbonate molecules. N_2 sorption results (Fig. 4b) show an enlarged specific surface area of 89.6 $m^2 \cdot g^{-1}$ with abundant mesopores, providing extra electrolyte reservoirs and transport channels. Stress–strain curves (Fig. 4c) reveal a volcano-type dependence of mechanical strength on MOF content: the tensile strength increases from 7.3 MPa (pristine) to 9.6 and 12.7 MPa for the 5 and 10 wt% samples, benefiting from the rigid filler and interfacial interactions, whereas the 15 wt% sample drops to 8.1 MPa owing to agglomeration-induced structural discontinuities. Hence, a moderate loading of 10 wt% balances reinforcement and homogeneity. The DFT-optimized adsorption configurations of EC and DMC solvent molecules on different separator substrates are displayed in Fig. 4d, intuitively confirming the stronger adsorption affinity of the Fe-Ti MOF toward carbonate electrolyte components, which is consistent with the superior wettability results.

3.5 Li^+ flux regulation and dendrite suppression

Temperature-dependent ionic conductivities are presented in Fig. 5a. At 30°C, PVDF-HFP/MOF-10 delivers the highest σ of 1.7×10^{-3} S cm^{-1} (vs. 8.3×10^{-4} S cm^{-1} for Celgard), and the Arrhenius fitting yields a reduced activation energy of 0.27 eV (vs. 0.32 eV for pristine PVDF-HFP and 0.38 eV for Celgard), indicating a lower energy barrier for Li^+ migration. More importantly, t_{Li^+} (Fig. 5b) increases from 0.24 (Celgard) and 0.33 (PVDF-HFP) to 0.56 for PVDF-HFP/MOF-10, which is direct evidence of the anion-anchoring effect: the Lewis-acidic Fe/Ti dual sites and the sub-nanometer channels of the MOF immobilize bulky PF_6^- anions while allowing fast Li^+ passage. This picture is corroborated by DFT calculations (Table S1): the adsorption energy of PF_6^- on the Fe–Ti MOF reaches − 8.73 eV, far exceeding those on the PVDF-HFP units (− 0.25 to − 1.44 eV) and on PP (− 1.69 eV), confirming the synergistically enhanced anion affinity of the bimetallic sites; the corresponding values for the single-metal Fe-MOF and Ti-MOF controls are compared in Fig. S3. In contrast, the Li^+ adsorption energy on the Fe–Ti MOF is far more moderate (− 2.91 eV), permitting facile hopping rather than trapping. The same trend holds for the carbonate solvents, whose adsorption energies on the Fe–Ti MOF (− 1.19 eV for EC and − 1.49 eV for DMC) greatly exceed those on PP (− 0.01 and − 0.02 eV) and on the PVDF-HFP units (− 0.02 to − 0.15 eV), rationalizing the superior electrolyte affinity of the composite separator.

These observations are rationalized by a flux-homogenization mechanism supported by the DFT adsorption energies (Fig. 5c, d): the elevated t_{Li^+} and the PF_6^--anchoring dual metal sites suppress anion depletion and the resulting space-charge field near the anode, so the local current density is homogenized and Li deposits uniformly instead of preferentially at protrusions. The Li^+ flux-regulation capability was directly assessed by galvanostatic plating/stripping in Li||Li symmetric cells at 1 mA cm^{-2} with 1 mAh cm^{-2} (Fig. 5e). The Celgard-based cell exhibits a gradually increasing overpotential and short-circuits after only 112 h, and the pristine PVDF-HFP cell survives 276 h, whereas the PVDF-HFP/MOF-10 cell maintains a stable, low voltage hysteresis of 16 mV for over 500 h without any sign of short circuit, demonstrating markedly improved interfacial stability. Thus, the separator functions as an active ion-redistribution layer rather than a passive membrane. Post-mortem SEM images of the cycled separators (Fig. 5f) visualize the underlying difference: the PVDF-HFP membrane shows surface cracking and lithium residue, whereas the PVDF-HFP/MOF-10 separator retains an intact, crack-free fibrous network.

3.6 Electrochemical performance of $LiFePO_4$||Li cells

The practical benefit of the composite separator was examined in $LiFePO_4$||Li cells cycled between 2.5 and 4.0 V. In the initial charge–discharge curves at 1 C (Fig. 6a), the PVDF-HFP/MOF-10 cell delivers the highest discharge capacity of 153 mAh g^{-1} with the smallest polarization (85 mV), compared with 138 and 145 mAh g^{-1} for the Celgard and pristine PVDF-HFP cells; all values approach the theoretical capacity of $LiFePO_4$ (170 mAh g^{-1}), indicating high active-material utilization. The rate performance (Fig. 6b) follows the same trend: at 10 C the PVDF-HFP/MOF-10 cell still retains 118 mAh g^{-1}, whereas the Celgard cell drops to 72 mAh g^{-1}, and the capacity recovers to 151 mAh g^{-1} when the rate returns to

1 C, evidencing excellent reversibility. This advantage at high rate is a direct consequence of the elevated t_Li⁺ and the reduced concentration polarization afforded by anion anchoring.

The long-term cycling stability of the LFP full cells was further evaluated at a constant 1 C rate (Fig. S4, Supporting Information). The PVDF-HFP/MOF-10 cell delivers a highly reversible discharge capacity of 141.2 mAh g^{-1} after 500 consecutive cycles, corresponding to an ultrahigh capacity retention of 92.3% with an average Coulombic efficiency exceeding 99.8% throughout the cycling process. In sharp contrast, the Celgard-based cell suffers from rapid capacity fading, retaining only 58.2% of its initial capacity after 500 cycles, while the pristine PVDF-HFP cell shows moderate degradation with 75.6% retention under the same conditions. This outstanding long-term cyclability originates from the sustained anion-anchoring effect of the Fe-Ti bimetallic MOF, which maintains homogeneous Li^+ flux, suppresses dendrite growth, and mitigates interfacial side reactions during prolonged cycling, consistent with the post-mortem interfacial characterization results. Wide-temperature operation was assessed by cycling at 20, 40, 60 and 80°C (Fig. 6c). The PVDF-HFP/MOF-10 cell maintains nearly unattenuated capacity across the whole range, benefiting from the thermal robustness of the composite separator, whereas the Celgard cell degrades severely above 60°C, consistent with its pronounced thermal shrinkage (Fig. 3b). CV curves (Fig. 6d) show sharper redox peaks and a smaller peak separation of 0.12 V for the composite separator, and EIS analysis (Fig. 6e, fitting parameters in Table S2) reveals the lowest charge-transfer resistance of 62 Ω, both indicating accelerated interfacial kinetics. The temperature-dependent ionic conductivities of the assembled cells (Fig. 6f) follow Arrhenius behaviour and confirm the reduced migration barrier of the composite separator. A comparison with recently reported functionalized separators (Table 1) highlights the competitiveness of the present system in terms of t_{Li^+}, symmetric-cell lifespan, and rate capability.

Table 1
Performance comparison of the present separator with recently reported functionalized separators for lithium batteries

Separator system	Cell system / voltage window	t_{Li^+}	Li||Li lifespan (h)	Capacity retention	Ref.
PVDF-HFP/Fe–Ti MOF (this work)	2.5–4.0	0.56	> 500	92.3% / 500 cycles (1 C)	—
PW_{12}@UiO-66-coated PP	NCM811||graphite (pouch)	0.75	1000	97% / 350 cycles (C/3)	[25]
UiO-66-F-coated PP	LFP||Li	—	> 2000	118 mAh g^{-1} @10 C	[13]
NH_2-ZIF-8 composite separator	LFP; NCM-333	0.72	4000 (5 mA cm^{-2})	71.9% (LFP, 5C, 500)	[26]

3.7 Post-cycling interfacial stability and working mechanism

To evaluate the interfacial durability, the cycled PVDF-HFP/MOF-10 separator was retrieved and characterized after 300 cycles, an intermediate stage of the 500-cycle test. SEM images show a well-preserved fibrous architecture without pore clogging, and Raman/XPS analyses confirm that the MOF framework and its Fe/Ti chemical states remain essentially unchanged, verifying the chemical robustness of the bimetallic framework in the carbonate electrolyte environment.

Based on all the above evidence, the working mechanism is summarized in Fig. 7. For the Celgard separator, unregulated anion motion produces a steep Li^+ concentration gradient and an inhomogeneous flux, which triggers dendritic deposition and, under fast-charging operation, accelerates interfacial degradation. In contrast, the Fe–Ti dual Lewis-acidic sites of the MOF strongly anchor PF_6^- anions (synergistically enhanced relative to single-metal sites), while the sub-nanometer channels sieve and redistribute Li^+; together with the highly wettable, thermally stable electrospun matrix, the composite separator homogenizes the Li^+ flux, enables flat and dense Li deposition, and sustains stable, fast-charging $LiFePO_4$ cycling.

4. Conclusions

In summary, an Fe–Ti bimetallic MOF was solvothermally synthesized and integrated into electrospun PVDF-HFP nanofiber membranes to construct a multifunctional separator for $LiFePO_4$ batteries. Combined XPS, single-particle EDS, and ICP-OES analyses unambiguously verified the framework-level coexistence and electronic coupling of the Fe and Ti centers (Fe/Ti = 0.108), which underpins the synergistic anion-anchoring capability of the dual Lewis-acidic sites. The optimized PVDF-HFP/MOF-10 separator simultaneously achieves outstanding thermal safety (5.8% shrinkage at 160°C and self-extinguishing behavior), superior electrolyte affinity (contact angle 18°), fast and selective ion transport ($\sigma = 1.7 \times 10^{-3}$ S cm^{-1}, $t_{Li^+} = 0.56$), and effective dendrite suppression (Li||Li symmetric cells stable for over 500 h with flat Li deposition). Consequently, $LiFePO_4$||Li cells deliver 153 mAh g^{-1} at 1 C with excellent rate capability up to 10 C, 92.3% capacity retention over 500 long-term cycles at 1 C, and nearly unattenuated capacity up to 80°C. This work establishes bimetallic-site engineering of MOF-functionalized separators as a viable route toward safe, fast-charging lithium batteries; scale-up fabrication and pouch-cell validation are underway to assess its practical potential.

Declarations

Acknowledgements This work was supported by the Open Project of the Application Research Center of Smart Energy Technology of Mianyang City College (Project No. ZHNY-2025-14; Contract No. 2025-330), the Startup Foundation for Introducing Talent of Meishan Vocational & Technical College (No. 2024RC06), the Key Laboratory of Fine Chemicals and Surfactants in Sichuan Provincial Universities (No. 2024JXY07). The authors extend their gratitude to Mr. Bin He from Scientific Compass (www.shiyanjia.com) for providing invaluable assistance with the Raman spectroscopy analysis.

Author contributions Keying Wu: conceptualization, investigation, writing—original draft, supervision, funding acquisition; Bing Luo: MOF synthesis, electrochemical measurements; Haitao Pu: structural characterization; Jing Chen: cell assembly and testing; Xingjian Liu: cell testing; Wenda Xie: supervision, writing—review and editing.

Funding This work was funded by the Open Project of the Application Research Center of Smart Energy Technology of Mianyang City College (Project No. ZHNY-2025-14; Contract No. 2025-330), the Startup Foundation for Introducing Talent of Meishan Vocational & Technical College (No. 2024RC06), and the Key Laboratory of Fine Chemicals and Surfactants in Sichuan Provincial Universities (No. 2024JXY07).

Data availability The data that support the findings of this study are available from the corresponding author upon reasonable request.

Competing interests The authors declare no conflict of interest.

Ethics approval Not applicable. This study did not involve human participants or animals.

Consent to participate and consent for publication Not applicable.

References

1. Tarascon JM, Armand M (2001) Issues and challenges facing rechargeable lithium batteries. Nature 414:359–367. https://doi.org/10.1038/35104644
2. Goodenough JB, Park KS (2013) The Li-ion rechargeable battery: a perspective. J Am Chem Soc 135:1167–1176. https://doi.org/10.1021/ja3091438
3. Liu J, Bao Z, Cui Y et al (2019) Pathways for practical high-energy long-cycling lithium metal batteries. Nat Energy 4:180–186. https://doi.org/10.1038/s41560-019-0338-x
4. Padhi AK, Nanjundaswamy KS, Goodenough JB (1997) Phospho-olivines as positive-electrode materials for rechargeable lithium batteries. J Electrochem Soc 144(4):1188–1194. https://doi.org/10.1149/1.1837571
5. Li W, Song B, Manthiram A (2017) High-voltage positive electrode materials for lithium-ion batteries. Chem Soc Rev 46:3006–3059. https://doi.org/10.1039/C6CS00875E
6. Nekahi A, Kumar AMR, Li X, Deng S, Zaghib K (2024) Sustainable $LiFePO_4$ and $LiMn_xFe_{1-x}PO_4$ (x = 0.1–1) cathode materials for lithium-ion batteries: a systematic review from mine to chassis. Mater Sci Eng R 159:100797. https://doi.org/10.1016/j.mser.2024.100797
7. Zhou H, Alujjage AS, Terese M, Fear C, Joshi T, Rikka VR, Jeevarajan JA, Mukherjee PP (2025) Effect of fast charging on degradation and safety characteristics of lithium-ion batteries with $LiFePO_4$ cathodes. Appl Energy 377:124465. https://doi.org/10.1016/j.apenergy.2024.124465
8. Fan X, Wang C (2021) High-voltage liquid electrolytes for Li batteries: progress and perspectives. Chem Soc Rev 50:10486–10566. https://doi.org/10.1039/D1CS00450F

9. Wu K, Tang H, Liu Y, Wang D, Jiang J, Yu L, Wang S, Chen L, Tang K (2026) Cation-anion synergistic stabilization at the heterointerface for ultra-stable 4.6 V $LiCoO_2$ cathodes. Ionics 32(4):4021–4033. https://doi.org/10.1007/s11581-026-06994-2
10. Zhang SS (2007) A review on the separators of liquid electrolyte Li-ion batteries. J Power Sources 164:351–364. https://doi.org/10.1016/j.jpowsour.2006.10.065
11. Arora P, Zhang Z (2004) Battery separators. Chem Rev 104:4419–4462. https://doi.org/10.1021/cr020738u
12. Lee H, Yanilmaz M, Toprakci O, Fu K, Zhang X (2014) A review of recent developments in membrane separators for rechargeable lithium-ion batteries. Energy Environ Sci 7:3857–3886. https://doi.org/10.1039/C4EE01432A
13. Li J, Yin G, Wang Y, Xiang Y, Yu N, Li X, Jiang Y, Xu M, Zhang X (2025) Enhancing the electrochemical performance and safety of lithium-ion battery via fluorinated MOF-based multifunctional separator. Chem Eng J 507:160148. https://doi.org/10.1016/j.cej.2025.160148
14. Jia S, Li Y, Chen Z, Li C, Duan C, Shen B (2023) Synthesis of PMIA/MIL-101(Cr) composite separators with high Li^+ transmission for boosting safety and electrochemical performance of lithium-ion batteries. J Colloid Interface Sci 647:12–22. https://doi.org/10.1016/j.jcis.2023.05.135
15. Zahn R, Lagadec MF, Hess M, Wood V (2016) Improving ionic conductivity and lithium-ion transference number in lithium-ion battery separators. ACS Appl Mater Interfaces 8:32637–32642. https://doi.org/10.1021/acsami.6b12085
16. Liang Y, Cheng S, Zhao J et al (2013) Heat treatment of electrospun polyvinylidene fluoride fibrous membrane separators for rechargeable lithium-ion batteries. J Power Sources 240:204–211. https://doi.org/10.1016/j.jpowsour.2013.04.019
17. Gopalan AI, Santhosh P, Manesh KM et al (2008) Development of electrospun PVdF–PAN membrane-based polymer electrolytes for lithium batteries. J Membr Sci 325:683–690. https://doi.org/10.1016/j.memsci.2008.08.047
18. Yang L, Cao J, Cai B, Liang T, Wu D (2021) Electrospun MOF/PAN composite separator with superior electrochemical performances for high energy density lithium batteries. Electrochim Acta 382:138346. https://doi.org/10.1016/j.electacta.2021.138346
19. Zhang Y, He R, Liu H, Liu H, Zhang X (2025) A Co-MOF decorated gel separator with high safety and stable electrochemical performance for lithium-sulfurized poly(acrylonitrile) batteries. Electrochim Acta 517:145757. https://doi.org/10.1016/j.electacta.2025.145757
20. Chen Z, Guan M, Cheng Y, Li H, Ji G, Chen H, Fu X, Awuye DE, Zhu Y, Yin X, Man Z, Wu C (2023) Boehmite-enhanced poly(vinylidene fluoride-co-hexafluoropropylene)/polyacrylonitrile (PVDF-HFP/PAN) coaxial electrospun nanofiber hybrid membrane: a superior separator for lithium-ion batteries. Adv Compos Hybrid Mater 6(6):219. https://doi.org/10.1007/s42114-023-00794-2
21. Liu H, Wang H, Yang F, Zou R, Hou CC, Xu Q (2025) Recent progress on metal–organic framework-based separators for lithium–sulfur batteries. J Mater Chem A 13:6124–6151. https://doi.org/10.1039/D4TA08756A

22. Huang Z, Noh J, Yu S, Zeng Y, Lin X, Bai S, Kang K (2025) Metal-organic frameworks for electrolytes and interfaces in rechargeable batteries: from liquid to solid-state systems. Adv Energy Mater 15(37):2502809. https://doi.org/10.1002/aenm.202502809
23. Chang Z, Yang H, Pan A, He P, Zhou H (2022) An improved 9 micron thick separator for a 350 Wh/kg lithium metal rechargeable pouch cell. Nat Commun 13:6788. https://doi.org/10.1038/s41467-022-34584-z
24. Qi C, Xu L, Wang J, Li H, Zhao C, Wang L, Liu T (2020) Titanium-containing metal–organic framework modified separator for advanced lithium–sulfur batteries. ACS Sustain Chem Eng 8(34):12968–12975. https://doi.org/10.1021/acssuschemeng.0c03536
25. Liu Y, Hou T, Zhang W et al (2025) Anion-repulsive polyoxometalate@MOF-modified separators for dendrite-free and high-rate lithium batteries. Interdiscip Mater 4(1):190–200. https://doi.org/10.1002/idm2.12225
26. Hao Z, Li W, Liu G, Qi S, Tang Y, Jin Y, Wang L, Lu C, Huang W, Cao S, He X (2026) Amino-functionalized MOF separators enabling anion-confined and Li^+-selective transport for ultra-stable and high-rate lithium metal batteries. Chem Eng J 534:175094. https://doi.org/10.1016/j.cej.2026.175094
27. Sanati S, Abazari R, Albero J et al (2021) Metal–organic framework derived bimetallic materials for electrochemical energy storage. Angew Chem Int Ed 60(20):11048–11067. https://doi.org/10.1002/anie.202010093
28. Chen L, Wang HF, Li C, Xu Q (2020) Bimetallic metal–organic frameworks and their derivatives. Chem Sci 11:5369–5403. https://doi.org/10.1039/D0SC01432J
29. Razaq R, Din MMU, Småbråten DR, Eyupoglu V, Janakiram S, Sunde TO, Allahgoli N, Rettenwander D, Deng L (2024) Synergistic effect of bimetallic MOF modified separator for long cycle life lithium–sulfur batteries. Adv Energy Mater 14:2302897. https://doi.org/10.1002/aenm.202302897
30. Shin J, Kim M, Cirera J, Chen S, Halder GJ, Yersak TA, Paesani F, Cohen SM, Meng YS (2015) MIL-101(Fe) as a lithium-ion battery electrode material: a relaxation and intercalation mechanism during lithium insertion. J Mater Chem A 3(8):4738–4744. https://doi.org/10.1039/C4TA06694D
31. Guo M, Li H (2021) The hydrolyzed MIL-88B(Fe) with improved surface area for high-capacity lithium ion battery. Front Energy Res 9:781008. https://doi.org/10.3389/fenrg.2021.781008

Figures

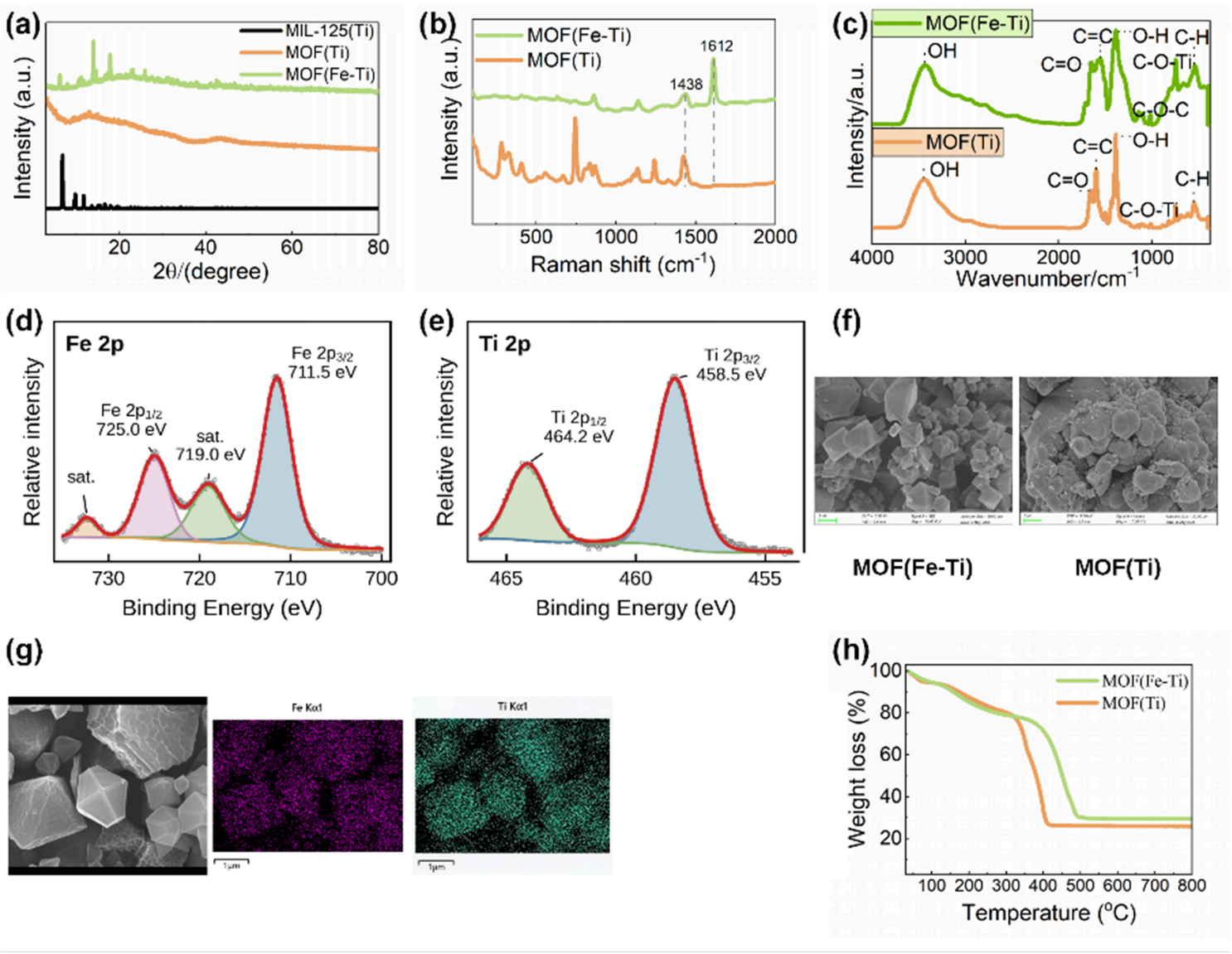


Figure 1

(a) XRD patterns of the Fe–Ti MOF, the single-metal Ti-MOF control, and the simulated reference; (b) Raman and (c) FT-IR spectra; high-resolution XPS spectra of (d) Fe 2p and (e) Ti 2p; (f) SEM images; (g) single-particle EDS elemental mapping showing Fe/Ti co-localization; (h) TGA curves. Full survey XPS spectra and N_2 sorption isotherms are provided in Figs. S1 and S2 of the Supplementary Information

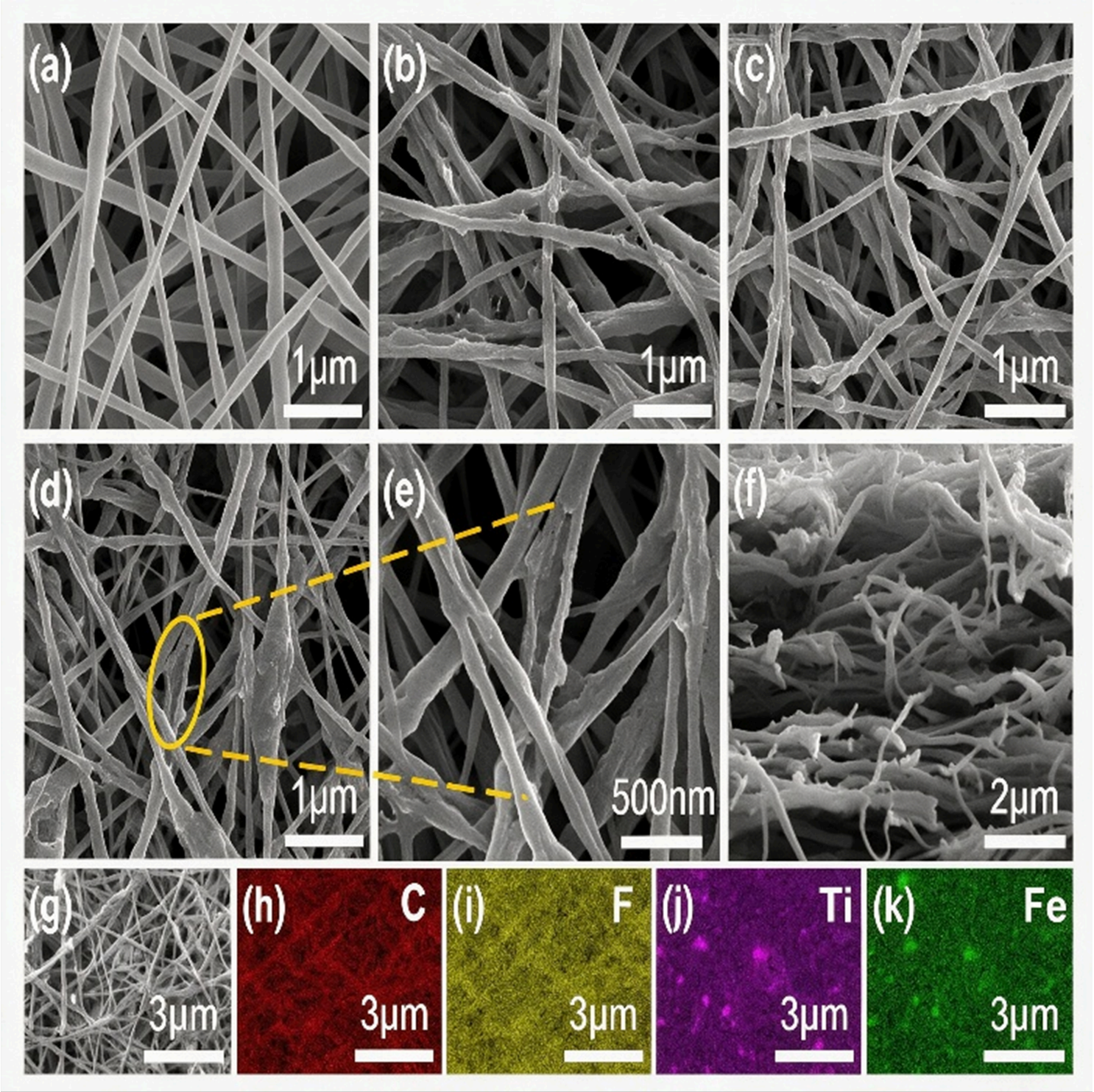


Figure 2

Morphology and elemental distribution of the composite separators. Surface SEM images of (a) pure PVDF-HFP, (b) PVDF-HFP/MOF-5, (c) PVDF-HFP/MOF-10, and (d) PVDF-HFP/MOF-15 nanofiber separators; (e) cross-sectional SEM image and (f, g) magnified surface SEM images of the PVDF-HFP/MOF-10 separator; (h–k) EDS elemental mapping of C, F, Ti and Fe in the PVDF-HFP/MOF-10 separator

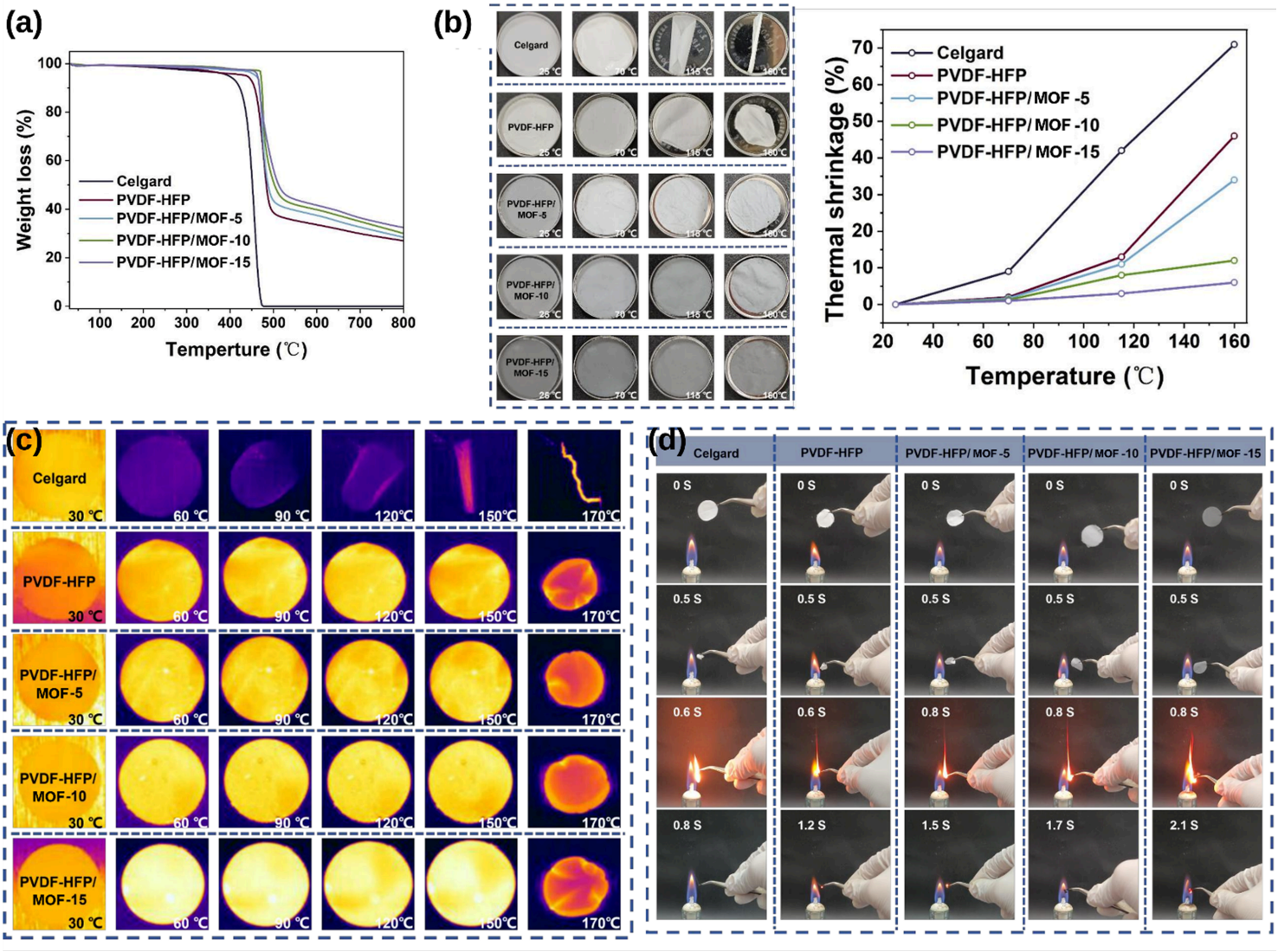


Figure 3

(a) TGA curves; (b) photographs and shrinkage-ratio curves of the separators after thermal treatment (each temperature held for 1 h); (c) FLIR thermal images (30–170 °C); (d) time-resolved combustion tests of Celgard, PVDF-HFP, and PVDF-HFP/MOF separators

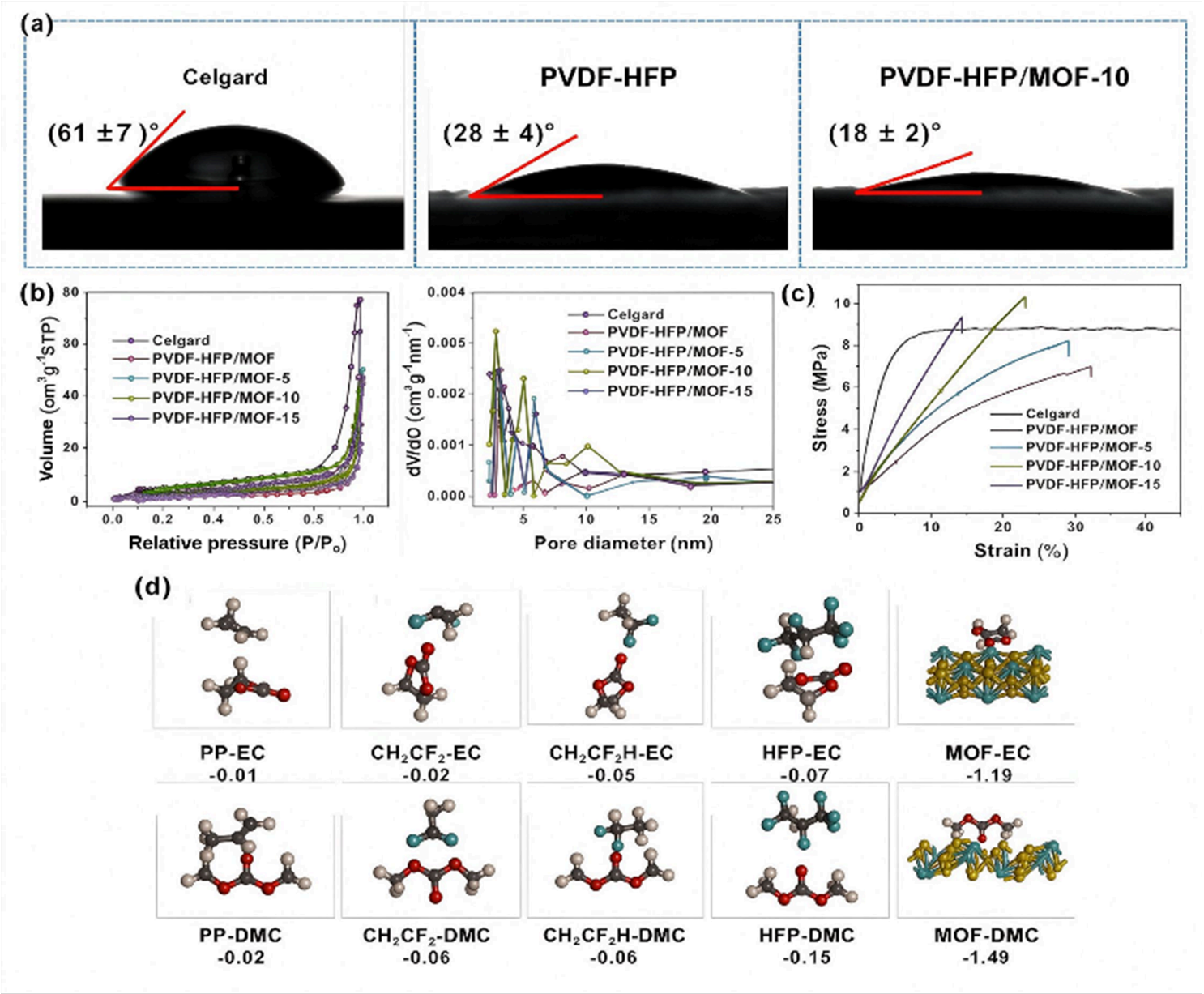


Figure 4

(a) Electrolyte contact angles; (b) N_2 adsorption–desorption isotherms and pore-size distributions; (c) tensile stress–strain curves; (d) DFT-optimized adsorption configurations of EC and DMC on PP, on the constituent units of PVDF-HFP, and on the Fe–Ti MOF, with the corresponding adsorption energies (eV)

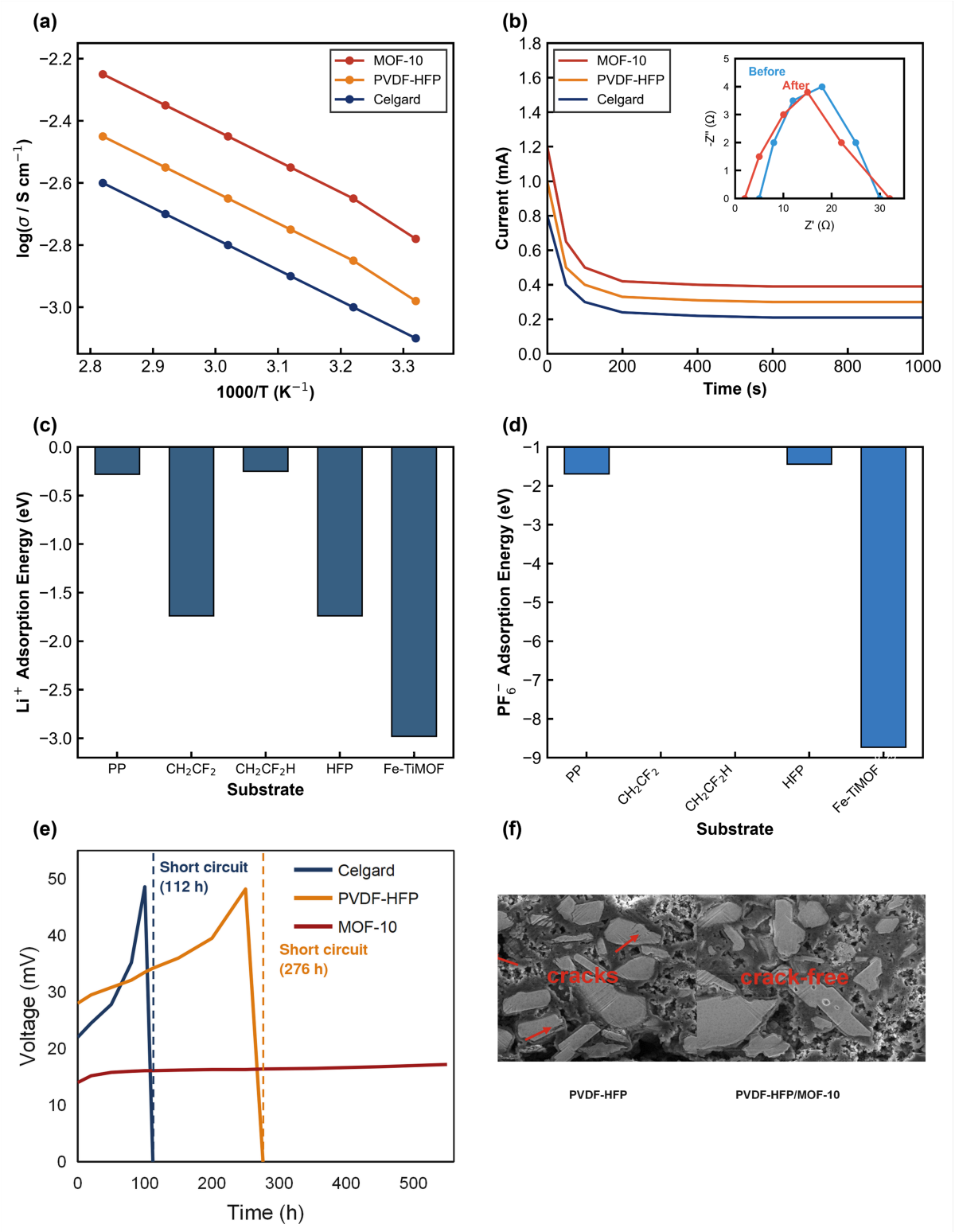


Figure 5

Ion-transport kinetics, interfacial energetics and dendrite suppression: (a) Arrhenius plots of log(σ) versus 1000/T with the fitted activation energies; (b) chronoamperometry profiles for t_{Li^+} determination (inset: EIS before and after polarization for PVDF-HFP/MOF-10); DFT adsorption energies of (c) Li^+ and (d) PF_6^- on PP, on the constituent units of PVDF-HFP, and on the Fe–Ti MOF; (e) voltage–time profiles of

Li||Li symmetric cells at 1 mA cm^{-2}/1 mAh cm^{-2}; (f) post-cycling SEM images of the PVDF-HFP and PVDF-HFP/MOF-10 separators

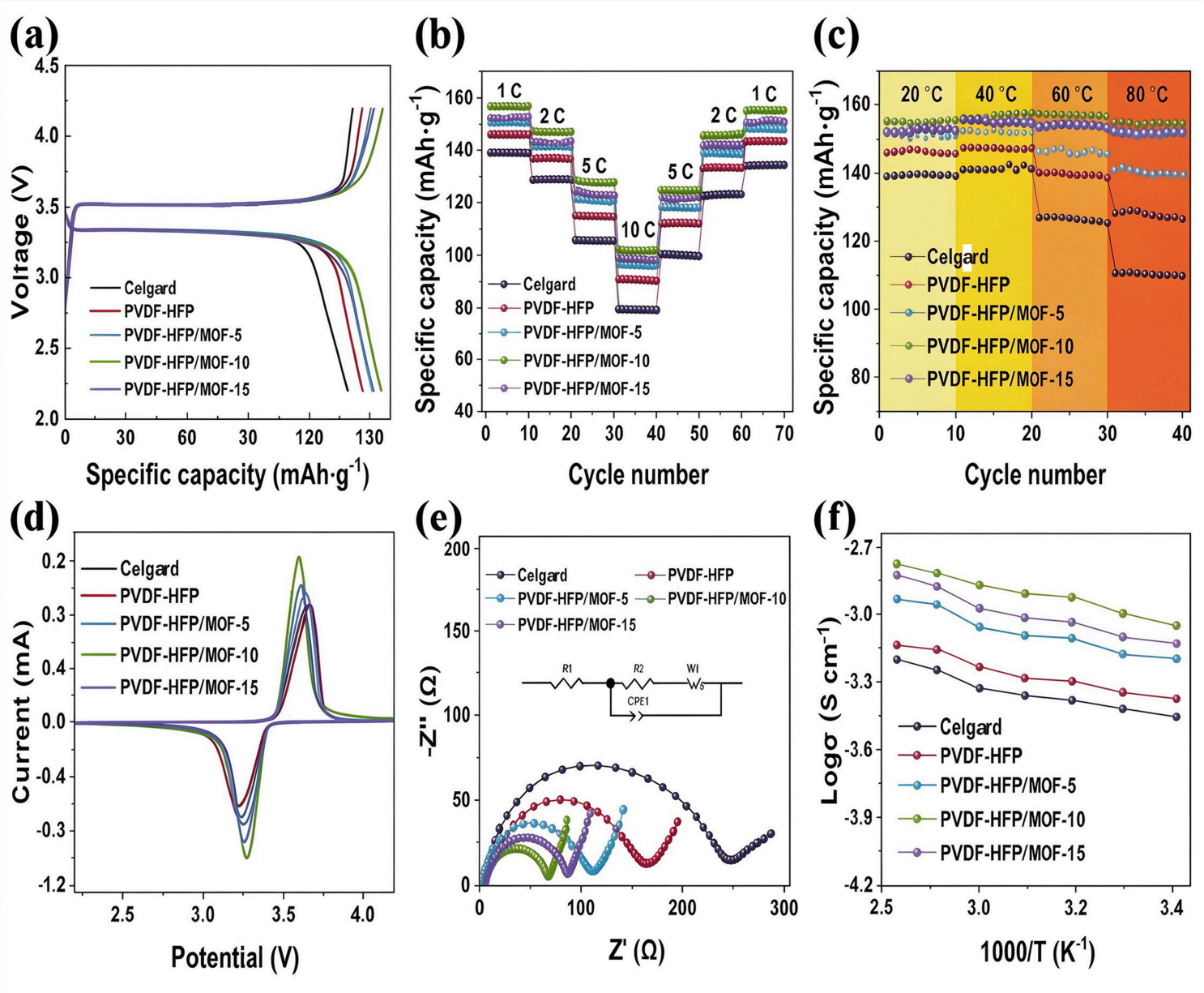


Figure 6

Electrochemical performance of $LiFePO_4$||Li cells (2.5–4.0 V) with different separators: (a) initial charge–discharge curves at 1 C; (b) rate capability from 1 C to 10 C; (c) cycling performance at 20, 40, 60 and 80 °C; (d) CV curves at 0.1 mV s^{-1}; (e) Nyquist plots with the equivalent circuit (inset); (f) Arrhenius plots of ionic conductivity

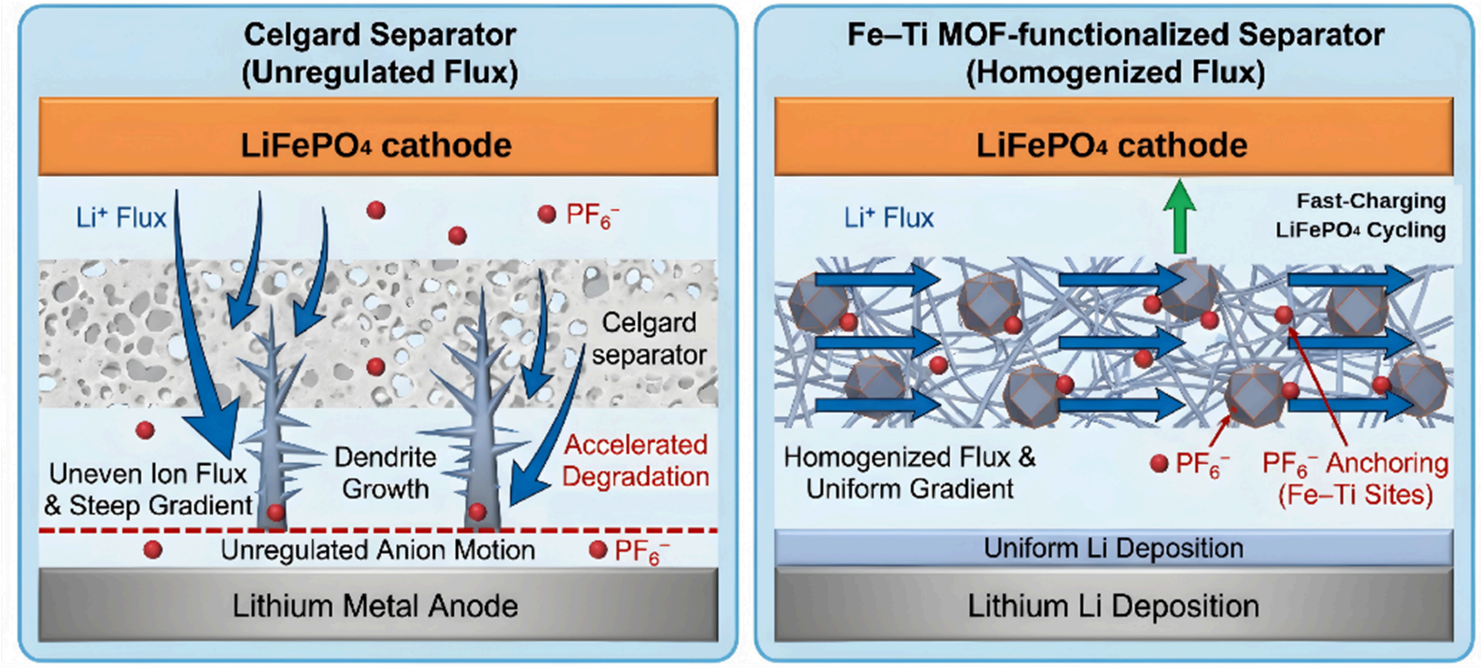


Figure 7

Schematic illustration of the Li^+ flux-regulation mechanism: uneven ion flux and dendrite growth across the Celgard separator versus PF_6^- anchoring, flux homogenization, and uniform Li deposition enabled by the Fe–Ti bimetallic MOF-functionalized separator

Supplementary Files

This is a list of supplementary files associated with this preprint. Click to download.

- SupportingInformation.docx